



Ultra-low-energy programmable non-volatile silicon photonics based on phase-change materials with graphene heaters

Zhuoran Fang¹✉, Rui Chen¹, Jiajiu Zheng¹ , Asir Intisar Khan² , Kathryn M. Neilson² , Sarah J. Geiger³, Dennis M. Callahan³, Michael G. Moebius³ , Abhi Saxena¹, Michelle E. Chen^{2,4}, Carlos Rios^{5,6}, Juejun Hu⁷ , Eric Pop^{2,4}  and Arka Majumdar^{1,8}✉

Silicon photonics is evolving from laboratory research to real-world applications with the potential to transform many technologies, including optical neural networks and quantum information processing. A key element for these applications is a reconfigurable switch operating at ultra-low programming energy—a challenging proposition for traditional thermo-optic or free carrier switches. Recent advances in non-volatile programmable silicon photonics based on phase-change materials (PCMs) provide an attractive solution to energy-efficient photonic switches with zero static power, but the programming energy density remains high (hundreds of attojoules per cubic nanometre). Here we demonstrate a non-volatile electrically reconfigurable silicon photonic platform leveraging a monolayer graphene heater with high energy efficiency and endurance. In particular, we show a broadband switch based on the technologically mature PCM $\text{Ge}_2\text{Sb}_2\text{Te}_5$ and a phase shifter employing the emerging low-loss PCM Sb_2Se_3 . The graphene-assisted photonic switches exhibited an endurance of over 1,000 cycles and a programming energy density of $8.7 \pm 1.4 \text{ aJ nm}^{-3}$, that is, within an order of magnitude of the PCM thermodynamic switching energy limit ($\sim 1.2 \text{ aJ nm}^{-3}$) and at least a 20-fold reduction in switching energy compared with the state of the art. Our work shows that graphene is a reliable and energy-efficient heater compatible with dielectric platforms, including Si_3N_4 , for technologically relevant non-volatile programmable silicon photonics.

In the past decade, programmable silicon photonic integrated circuits (PICs) have moved from traditional applications, such as optical interconnects¹ and signal processing², to emerging fields, such as optical neural networks³, quantum information processing⁴ and light detection and ranging⁵. All these applications require numerous optical components and switches. As PICs are scaled up, the physical size and energy consumption of individual photonic switches become increasingly critical. However, the traditional means of tuning silicon PICs, including thermo-optic⁶ and free carrier dispersion effects⁷, suffer from a large programming energy, large form factors, a volatile nature and a small change in the complex refractive index ($\Delta n < 0.01$). Recent progress in hybrid silicon photonics⁸ could circumvent some of these limitations. For example, III–V/silicon modulators⁹ based on the plasma dispersion and band-filling effects achieve a small half-wave voltage-length product ($V_\pi L$) of 0.047 V cm , silicon–lithium niobate modulators based on the Pockels effect afford low-energy (170 fJ) and ultra-fast (70 GHz) switching speed¹⁰ and silicon–organic hybrid modulators operate at sub-femtojoule per bit¹¹. Nevertheless, most approaches are still based on volatile field effects with limited complementary metal oxide semiconductor (CMOS) compatibility^{9–11}. In contrast, non-volatile programming of PICs can greatly improve the energy efficiency because the static power consumption is zero, leading to true ‘set-and-forget’-type switches¹². In particular, chalcogenide-based phase-change materials (PCMs) can afford a

feasible solution¹³ as a result of a non-volatile microstructural phase transition¹⁴, large contrast in complex refractive index¹⁵ (typically $\Delta n \geq 1$) and CMOS compatibility¹³. In fact, PCMs have recently attracted considerable attention in the creation of programmable PICs with applications in, for example, photonic switches^{16–19}, photonic memory²⁰ and optical computing^{21,22}.

So far, the majority of the reported phase-change PICs have employed optical switching for reconfiguration^{17,20,23}. In particular, high cyclability ($>4,000$)²⁴, strong optical phase modulation ($\sim 2\pi$) and low insertion loss ($\sim 0.5 \text{ dB}$) have been demonstrated by laser switching Sb_2Se_3 on silicon-on-insulator (SOI) waveguides²³. Compared with optical switching, electrical switching provides a more attractive solution^{13,25} for ease of scaling and the ability to switch a large volume of PCMs. Recent advances in electrically reconfigurable PCM-integrated PICs^{16,18,26–29} have revealed that electrical switching by an external heater is a more effective approach than ‘memory switching’^{30,31}, which is typically performed in electronic phase-change memory devices. ‘Memory switching’ switches only the volume that is necessary for conduction to change; hence, the optical contrast is very small ($\sim 0.6\%$)³². In contrast, switching by external heaters, such as forward-biased p-type/intrinsic/n-type (PIN) diodes¹⁶, doped silicon^{18,26} and indium tin oxide (ITO)^{27–29}, enables a larger volume of PCMs to undergo a phase transition, allowing high extinction ratio photonic switches. Despite the progress, fundamental challenges still

¹Department of Electrical and Computer Engineering, University of Washington, Seattle, WA, USA. ²Department of Electrical Engineering, Stanford University, Stanford, CA, USA. ³The Charles Stark Draper Laboratory, Cambridge, MA, USA. ⁴Department of Materials Science and Engineering, Stanford University, Stanford, CA, USA. ⁵Department of Materials Science and Engineering, University of Maryland, College Park, MD, USA. ⁶Institute for Research in Electronics and Applied Physics, University of Maryland, College Park, MD, USA. ⁷Department of Materials Science and Engineering, Massachusetts Institute of Technology, Cambridge, MA, USA. ⁸Department of Physics, University of Washington, Seattle, WA, USA. ✉e-mail: rogefzr@uw.edu; arka@uw.edu

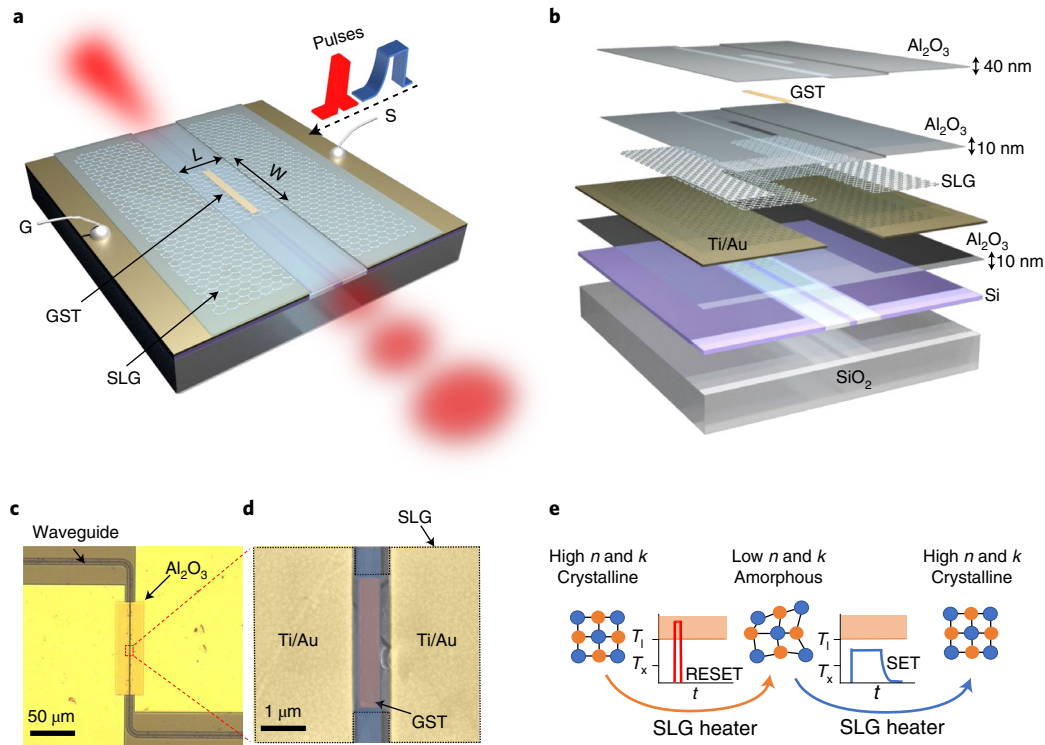


Fig. 1 | A graphene-PCM reconfigurable silicon photonic platform. **a**, Schematic of the device structure. SLG, single-layer graphene; S, signal electrode; G, ground electrode. **b**, The layered structure of the device. **c**, Optical micrograph of the waveguide switch. **d**, False-colour SEM image of the waveguide area, where the GST is patterned. The SLG area is indicated by the black dashed lines. **e**, Operating principle of the device. k , extinction coefficient; t , time.

exist for electrical switching using external heaters. First, the programming energy density remains high (hundreds of attojoules per cubic nanometre), far exceeding the theoretical limit¹⁴ of $\sim 1.2 \text{ aJ nm}^{-3}$. Second, the switching current and voltage typically reach tens of milliamperes and more than 5 V, considerably higher than the CMOS-driving currents and voltages (considering 5 V CMOS technologies³³). Lastly, so far, no reliable transparent heaters have been reported that are compatible with dielectric platforms such as silicon nitride (Si_3N_4), a leading integrated photonic platform³⁴. Polysilicon heaters have been used to thermally tune Si_3N_4 waveguides³⁵, but they are optically decoupled from the waveguides, leading to high power consumption ($>100 \text{ mW}$) and slow response speed ($\sim 10 \text{ kHz}$). Transparent conducting oxides, such as ITO, have been investigated^{27–29,36} for tuning PCMs on both Si and Si_3N_4 waveguides, but the reversible switching is still unsatisfactory. However, the switching of PCMs by graphene can provide outstanding performance²⁵, and the underlying physical mechanism was recently studied in a proof-of-principle device³⁷.

In this study, we leveraged these advances and state-of-the-art nanofabrication to design a highly optimized device that demonstrates the technological feasibility of non-volatile, electrically reconfigurable, hybrid PCM–silicon photonic platforms using a monolayer graphene heater. We first designed an ultra-compact broadband waveguide switch covering the whole telecommunication C-band based on absorption modulation using $\text{Ge}_2\text{Sb}_2\text{Te}_5$ (GST). The photonic switch was only $4.73 \mu\text{m}$ long and operated at a CMOS-driving current ($\leq 2.78 \text{ mA}$) and voltage ($\leq 5 \text{ V}$)³³. Then, we employed the newly introduced low-loss PCM Sb_2Se_3 (ref. ²⁴) to demonstrate a graphene-assisted phase shifter using a micro-ring resonator that supports 14 distinct optical phase levels. The photonic switches showed ultra-low programming energy density ($8.7 \pm 1.4 \text{ aJ nm}^{-3}$) and high endurance ($>1,000$ cycles). Such high energy efficiency is possible because the atomically thin graphene,

which exhibits high thermal conductivity and ultra-low heat capacity, considerably reduces the thermal mass needed to actuate the phase transition.

A graphene-PCM reconfigurable platform in silicon photonics

Our graphene-PCM hybrid switching platform consisted of a patterned graphene bridge across a planarized 220 nm SOI waveguide (Fig. 1a,b; for additional fabrication details, see Methods and Supplementary Fig. 1). The layered view in Fig. 1b shows that the PCM sits above the graphene, which is transferred onto the waveguides. The 40-nm-thick top Al_2O_3 layer encapsulates both the PCM and graphene to prevent oxidation and PCM reflowing during switching. There is an additional 10 nm atomic-layer-deposited (ALD) Al_2O_3 spacer between the graphene and the PCM that isolates the two materials. This spacer prevents the rupture of graphene due to the tension caused by the volume expansion and contraction of the PCM on switching. The metal contacts are placed only 300 nm away from the 500-nm-wide waveguide to reduce the graphene resistance while maintaining a low experimental metallic absorption loss of $0.002 \pm 0.001 \text{ dB } \mu\text{m}^{-1}$. Such a low Ohmic loss, despite the proximity of the metals to the waveguides, is made possible by the geometry of the planarized waveguide (Supplementary Fig. 2a), which keeps the optical mode away from the metal plane and minimizes the evanescent interaction. The graphene has a large contact area ($9.75 \mu\text{m} \times 100 \mu\text{m}$) with the metals to reduce the contact resistance, and it narrows at the bridge to restrict the current flow to the PCM region and to minimize absorptive loss from the graphene. The bridge region has a width W designed to be 200 nm longer than the length of the PCM and a length L fixed at $1.1 \mu\text{m} = (0.3 \mu\text{m} \times 2) + 0.5 \mu\text{m}$. An optical micrograph of the fabricated device is shown in Fig. 1c, and Fig. 1d shows the false-colour scanning electron microscopy (SEM) image of a $2.85 \mu\text{m} \times 400 \text{ nm}$

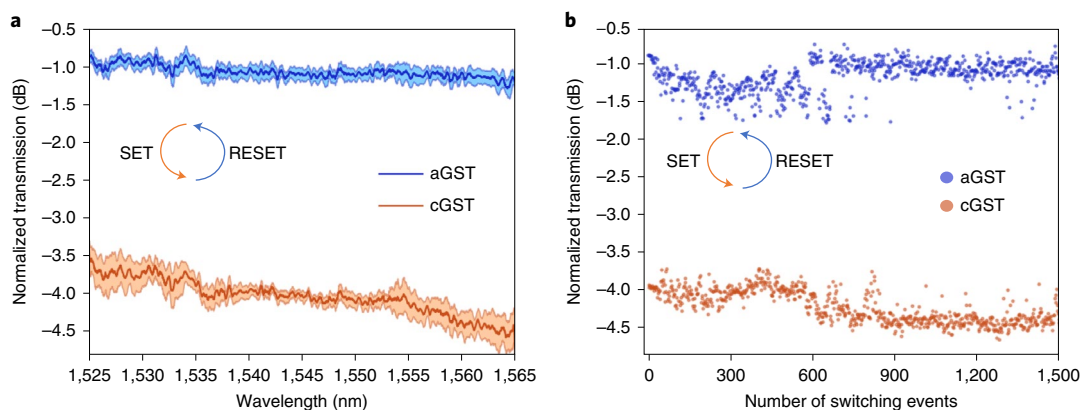


Fig. 2 | Graphene-assisted broadband waveguide switch based on GST. **a**, Reversible switching of GST on an SOI waveguide using a graphene heater. The switching conditions were 3 V, 100 μ s pulse width and 120 μ s trailing edge for SET, and 5 V, 400 ns pulse width and 8 ns trailing edge for RESET. Eight consecutive cycles were performed; the shaded area indicates the standard deviation of the cycles and the solid line indicates the average. The device spectrum is normalized to the spectrum of a bare waveguide. **b**, Cyclability of the switch for 1,500 switching events. The pulse conditions were the same as in **a**. Each pulse was temporally separated by 2 s to ensure long thermal relaxation. The transmission is normalized to the transmission of a bare waveguide. cGST, crystalline GST; aGST, amorphous GST.

GST patch on the waveguide, revealing the excellent accuracy of the lithographic alignment.

Figure 1e illustrates the operating principle of the graphene-PCM photonic switch. By applying a high amplitude and short voltage pulse, also known as a ‘RESET’ pulse, across the graphene bridge, the PCM is heated above its melting temperature T_1 and rapidly quenched by removing the excitation. The melt–quench operation induces the amorphization of the PCM and transforms the PCM into a transparent and lower refractive index state. Application of a low amplitude and long voltage pulse, also known as a ‘SET’ pulse, across the graphene heater heats the PCM above its crystallization temperature T_x and below the melting point to return the PCM to its crystalline state. The long trailing edge ensures slow cooling of the material to complete the crystallization. The material is then restored to the higher absorption and refractive index crystalline state. The two devices discussed below leverage the absorption and refractive index modification of the PCM actuated by graphene heaters to realize a broadband on/off switch and a low-loss phase shifter, respectively.

Graphene-assisted broadband waveguide switch based on GST

We first explored a broadband waveguide switch based on the absorption modulation of GST. GST exhibited a large change in complex refractive index upon phase transition, giving rise to a remarkable modification of the optical mode of the GST-clad waveguide (Supplementary Fig. 2). Although the strong optical absorption of GST in the crystalline state makes it undesirable for phase-only control in the near infrared, the amplitude modulation of GST across a wide wavelength range is attractive for applications such as photonic memory²⁰ and optical computing³⁸. Figure 2a shows the reversible switching of the waveguide spectrum between low (crystalline GST) and high (amorphous GST) transmission states for eight consecutive cycles using the device structure shown in Fig. 1c,d. The shaded regions of the spectra indicate the standard deviation for the eight switching cycles, clearly revealing excellent cycle-to-cycle reproducibility. A contrast of 3 dB in transmission can be observed across the entire telecommunication C-band with a 4.73- μ m-long, 23-nm-thick GST. Temporal trace measurements (Supplementary Fig. 4a) confirmed that the change was non-volatile and hence caused by the GST. The 0.74 dB μ m⁻¹ optical contrast is slightly lower than that for GST placed directly on top

of the waveguides¹⁶ (in our device a 20 nm Al₂O₃ spacer is placed between the GST and waveguide), but agrees well with the optical mode simulations (Supplementary Fig. 2a). Heat transfer simulation also confirmed that the temperature reached the required threshold temperatures for both the crystallization and amorphization of GST (Supplementary Fig. 2b). The total switching energy for the amorphization was 5.55 nJ, corresponding to an energy density of 127.6 aJ nm⁻³, and the energy dissipated by the graphene heater alone (that is, excluding the power loss at the contact resistance) was only 0.380 \pm 0.062 nJ, equivalent to an energy density of 8.74 \pm 1.42 aJ nm⁻³ (for details on estimating the graphene sheet resistance and switching power, see Supplementary Section 3). This represents a >20-fold reduction in the programming energy density compared with the state of the art³⁷ and within an order of magnitude of the \sim 1.2 aJ nm⁻³ fundamental limit¹⁴. Finally, we proved the high endurance of the device by performing 1,500 switching events on the graphene–GST photonic switch (Fig. 2b). An \sim 0.5 dB improvement in switching contrast was observed at around the 600th switching event (pulse conditions remain unchanged), which is likely attributable to a larger crystalline domain forming after the initial ‘conditioning’ steps²⁰. It has previously been found that the initial pulsing of PCMs could give rise to ordered structures that act as seeds for subsequent crystal growth with minimal nucleation³⁹. As a result, a larger volume of the PCM can be switched or ‘activated’.

Graphene-assisted low-loss phase shifter based on Sb₂Se₃ in a micro-ring resonator

Phase shifters are frequently used in PICs to realize Mach–Zehnder modulators and 1 \times 2 or 2 \times 2 switches. The large optical absorption of GST in the crystalline state prohibits its use for phase-only modulation. In this study, we employed the recently reported^{23,24} low-loss PCM Sb₂Se₃ to realize a graphene-assisted non-volatile phase shifter in a micro-ring resonator. We harnessed the transparent window of Sb₂Se₃ in the near infrared, where a negligible insertion loss of 0.002 \pm 0.002 dB μ m⁻¹ of the Sb₂Se₃-loaded waveguide was extracted using a cut-back method at 1,550 nm (Supplementary Fig. 5). A schematic of the device is illustrated in Fig. 3a, an optical micrograph of the device is shown in Fig. 3b and a false-colour SEM image of a 6- μ m-long, 400-nm-wide, 30-nm-thick Sb₂Se₃ patch on the waveguide is shown in Fig. 3c. Figure 3d shows the reversible tuning of a micro-ring resonance at 1,549 nm; the spectra of three

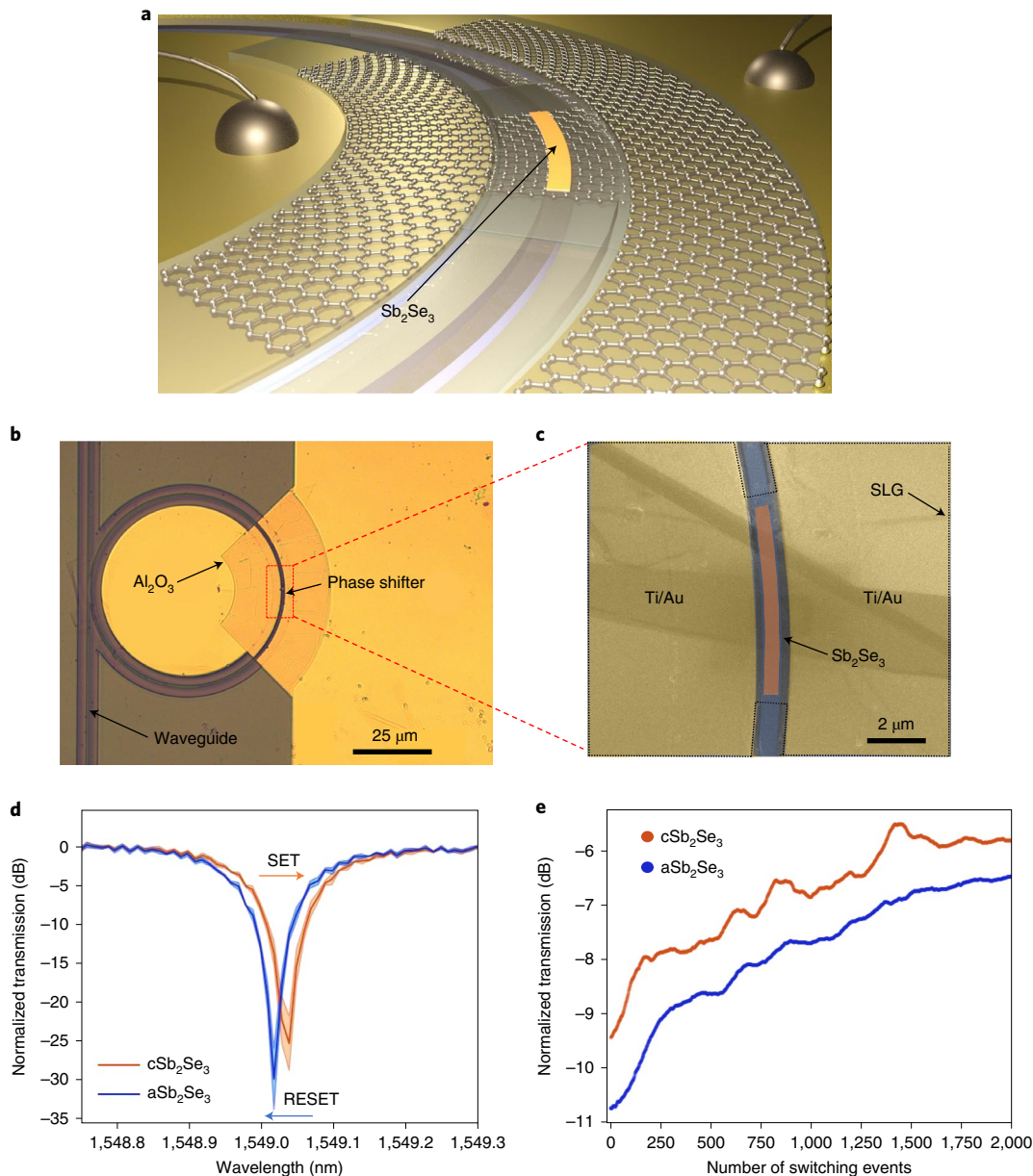


Fig. 3 | Graphene-assisted phase shifter based on Sb_2Se_3 in a micro-ring. **a**, Schematic of the graphene- Sb_2Se_3 phase shifter in a micro-ring. Note that an additional 10 nm sputtered SiO_2 layer is used to encapsulate the Sb_2Se_3 . Such SiO_2 capping is not used for GST. **b**, Optical micrograph of the micro-ring resonator integrated with a phase shifter. **c**, False-colour SEM image of the micro-ring area, where the Sb_2Se_3 is patterned. The graphene area is indicated by the black dashed lines. **d**, Reversible switching of Sb_2Se_3 using a graphene heater on micro-rings. The switching conditions were 4 V, 100 μs pulse width and 120 μs trailing edge for SET, and 6.8 V, 400 ns pulse width and 8 ns trailing edge for RESET. Three consecutive cycles are plotted; the shaded areas indicate the standard deviation of the cycles and the solid lines indicate the average. The spectra are normalized to the spectrum of a bare waveguide. **e**, Cyclability of the switch for 2,000 switching events. The switching conditions were 4 V, 100 μs pulse width and 120 μs trailing edge for SET, and 6.4 V, 400 ns pulse width and 8 ns trailing edge for RESET. Each pulse was temporally separated by 2 s to ensure long thermal relaxation. The transmission is normalized to the transmission of a bare waveguide. The data have been filtered by a 50-point moving average to reduce the fluctuation caused by thermal noise.

cycles are plotted and the shaded regions indicate the standard deviations of the cycles.

The total switching energy for amorphization was 9.25 nJ (128.4 aJ nm^{-3}) and the energy dissipated by the graphene heater alone (that is, excluding the power loss at the contact resistance) was only $0.57 \pm 0.09 \text{ nJ}$ and $7.9 \pm 1.3 \text{ aJ nm}^{-3}$ (for details on estimating the graphene sheet resistance and switching power, see Supplementary Section 3). A maximum resonance shift of 0.021 nm was extracted, which corresponds to a phase shift of 0.00822π and $V_{\pi}L$ of 0.496 V cm (assuming a switching voltage of 6.8 V), representing a

threefold improvement compared with the state-of-the-art silicon p-type/n-type (PN) phase shifter⁴⁰. The phase shift matches the simulation (Supplementary Fig. 2), but is smaller than the recently reported value¹⁸ due to the intrinsic smaller index change in our Sb_2Se_3 and the use of the 20 nm Al_2O_3 spacer. We believe that the phase modulation can be further improved with higher quality Sb_2Se_3 and a thinner spacer. The increase in the insertion loss (IL) of Sb_2Se_3 in the crystalline state was extracted by fitting the Q factor of the resonances and was estimated to be $0.006 \pm 0.002 \text{ dB } \mu\text{m}^{-1}$. The IL of the metal and graphene was estimated to be $0.002 \pm 0.001 \text{ dB } \mu\text{m}^{-1}$

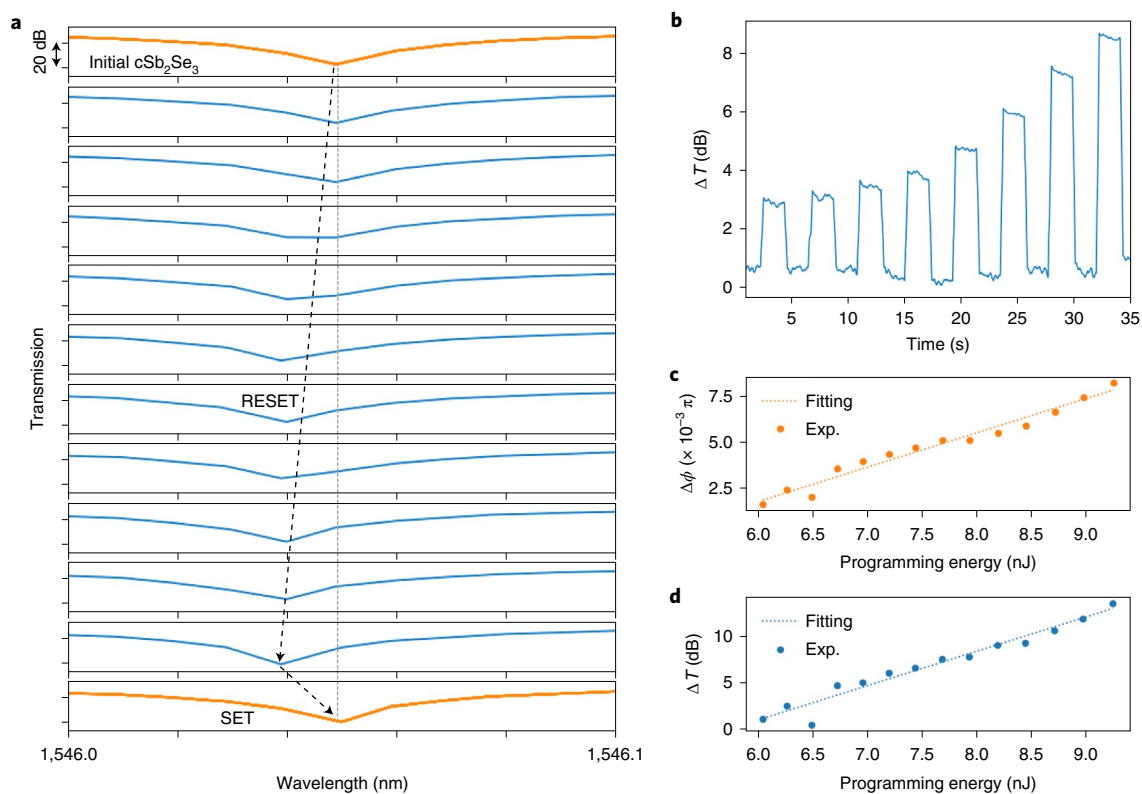


Fig. 4 | Quasi-continuous phase modulation using the graphene-Sb₂Se₃ phase shifter. **a**, Quasi-continuous tuning of micro-ring resonance by step amorphization. The SET conditions were 4 V, 100 μ s pulse width and 120 μ s trailing edge. For RESET, the amplitude was increased monotonically from 5.5 V to 6.4 V, and the pulse width and trailing edge were fixed at 400 ns and 8 ns, respectively. **b**, Temporal trace of a continuous programming iteration with a monotonically increasing RESET pulse amplitude from 5.5 V to 6.9 V followed by a SET pulse. Eight transmission levels are clearly resolved. The pulse width and trailing edge of the RESET pulse were fixed at 400 ns and 8 ns, respectively. The SET conditions were the same as in **a**. **c**, Change in phase shift ($\Delta\phi$) with programming energy. Fourteen phase levels can be resolved, with the phase shift increasing linearly with programming energy. Exp., experimental. **d**, Change in transmission caused by the variation in the phase shift with programming energy. Fourteen transmission levels can be resolved. The transmission contrast increases linearly with the programming energy, matching very well with **c**.

and $0.047 \pm 0.006 \text{ dB } \mu\text{m}^{-1}$, respectively, from fitting the micro-ring spectra after each overlay step. The total IL was only $\sim 0.33 \text{ dB}$ for a device with a length of $6 \mu\text{m}$. The graphene IL is slightly lower than the loss measured in a similar graphene-on-micro-ring structure⁴¹, for which an IL of $\sim 0.07 \text{ dB } \mu\text{m}^{-1}$ was extracted. The reduction in the graphene IL in our work is likely attributable to a lower carrier density and the 10 nm ALD Al₂O₃ spacer between the graphene and the waveguides, compared with the 3-nm-thick hexagonal boron nitride used in previous work⁴¹. Optical losses in graphene can be further suppressed by electrical gating to the Pauli blocking region^{42,43}.

Lastly, we demonstrated excellent endurance of the device by performing 2,000 switching events on the phase shifter (Fig. 3e). The laser wavelength was slightly detuned from the resonance wavelength to mitigate transmission fluctuations from the thermal drift (Methods). The gradual increase in transmission observed with cycling time was caused by the temperature-induced drift of the resonance wavelength away from the initial laser wavelength. Comparison of the spectrum of the as-fabricated micro-ring with that measured after 1,100 continuous cycles (Supplementary Fig. 6) showed that there was no broadening of the resonance peak, implying that the cycling did not induce any damage in the device. The temporal trace recorded after 1,100 cycles (Supplementary Fig. 4b) still showed a large optical contrast of 7 dB, as the laser wavelength was parked near the resonance. Transmission measurements taken between the switching events (duration of 2 s) indicated that the change was non-volatile and was indeed caused by Sb₂Se₃. The transient

response of the switching was characterized using a 150 MHz fast photoreceiver (Supplementary Fig. 9). Next, we compared our graphene-PCM hybrid platform with other electrical switching approaches in PCM-based photonics. Supplementary Fig. 10 clearly shows that our graphene-PCM switch not only exhibits one of the highest endurance (>1,000 cycles), but also produces the lowest switching energy density ($8.7 \pm 1.4 \text{ aJ nm}^{-3}$) reported so far. Finally, we compared our electrical switching study with previously reported optical switching data (Supplementary Table 2 in Supplementary Section 11).

Quasi-continuous multilevel phase modulation using the graphene-Sb₂Se₃ phase shifter

It is well known that PCMs can support multilevel operation, and this property is widely exploited in electronic memory³¹, photonic memory⁴⁴ and most recently in optical neural networks²². After realizing bistable switching, we further found that the phase shifter can be tuned quasi-continuously to attain multiple optical phase levels by controlling the programming energy. Figure 4a shows that as the programming voltage was monotonically increased in steps of 0.1 V from 5.5 V to 6.4 V (the pulse width and trailing edge were fixed at 400 ns and 8 ns, respectively), the resonance dip shifted gradually to a shorter wavelength, with the intermediate states corresponding to partially amorphous PCMs. This effect was caused by an increasingly larger hotspot in the centre of the heater, resulting in an increasingly larger area of the PCM being amorphized. As a result, the resonance dip shifted gradually to a shorter wave-

length, with these intermediate states corresponding to partially amorphous PCMs. After ten pulses of increasing amplitude, a SET pulse of 4 V (100 μ s pulse width and 120 μ s trailing edge) was used to return the resonance to the original position. The resonance wavelength of the SET state perfectly matched the resonance wavelength of the initial crystalline state, as indicated by the grey dashed line in Fig. 4a. The time dynamic response was investigated by increasing the programming voltage in increments of 0.2 V from 5.5 V to 6.9 V, and the transmission was continuously monitored with respect to time, as shown in Fig. 4b. After each RESET operation, the PCM returned to the initial crystalline state using the same SET pulse of 4 V. Eight distinct transmission levels could be clearly resolved with \sim 1 dB contrast between adjacent levels. To better quantify the multilevel phase modulation, we extracted the phase shift from the change in the resonance wavelength from each RESET pulse and plotted the phase shift against the programming energy (Fig. 4c). Fourteen phase levels were attained by increasing the programming energy from 6 nJ to 9.5 nJ, with the phase increasing linearly with the programming energy. Figure 4d shows that the resulting change in transmission from the phase modulation matches very well with Fig. 4c. The reproducibility of the multilevel operation was evaluated for five iterations (Supplementary Fig. 11b) and showed that although the transmission levels were not entirely deterministic, the mean transmission increased with the programming energy almost linearly. Similarly, multilevel operations could also be realized in the graphene-GST waveguide switch, for which seven distinct transmission levels were obtained (Supplementary Fig. 11a). We point out that, although not demonstrated in the current work, multilevel operation attained by step crystallization is also possible by adjusting the pulse amplitude and width, as shown by others^{20,28,31}.

Conclusion

We have reported two examples of non-volatile, electrically switchable, silicon photonic platforms leveraging a monolayer graphene heater: a GST-based broadband waveguide switch and a Sb₂Se₃-clad phase shifter. We achieved an ultra-low programming energy density (8.7 ± 1.4 aJ nm⁻³) and high endurance (>1,000 cycles) at CMOS-driving voltage (\leq 5 V) and current (\leq 2.78 mA). Our results prove that graphene is not only a reliable heater that can be controlled by CMOS electronics, but also compatible with dielectric platforms, including Si₃N₄, and can potentially be used on arbitrary substrates. We believe that further advances and optimization can come from the following sources: reducing the insertion loss of graphene by electrical gating to the Pauli blocking region^{42,43}, reducing the graphene contact resistance and contact area using one-dimensional edge contacts⁴⁵ and improving the phase modulation of the Sb₂Se₃ phase shifter using higher quality Sb₂Se₃^{18,23} and a thinner Al₂O₃ spacer. Additionally, graphene transfer is not yet available in commercial CMOS foundries, although wafer-scale synthesis, transfer and integration with photonic devices have been reported^{46,47}. Wafer-scale graphene transfer can be fully automated and it is the only step that needs to be added between the planarization of silicon waveguides and metallization in a standard CMOS process⁴⁸. Recent reports on graphene-based silicon photonic devices^{41,43} have described remarkable performance, superior to their counterparts in monolithic platforms, making full integration of wafer-scale graphene transfer with the current foundry processes highly attractive. We also note that graphene transfer and patterning processes happen at relatively low temperature and do not affect the underlying silicon photonic platform.

Online content

Any methods, additional references, Nature Research reporting summaries, source data, extended data, supplementary information, acknowledgements, peer review information; details of author contributions and competing interests; and statements of

data and code availability are available at <https://doi.org/10.1038/s41565-022-01153-w>.

Received: 17 December 2021; Accepted: 13 May 2022;

Published online: 04 July 2022

References

- Cheng, Q., Bahadori, M., Glick, M., Rumley, S. & Bergman, K. Recent advances in optical technologies for data centers: a review. *Optica* **5**, 1354–1370 (2018).
- Pérez, D. et al. Multipurpose silicon photonics signal processor core. *Nat. Commun.* **8**, 636 (2017).
- Shen, Y. et al. Deep learning with coherent nanophotonic circuits. *Nat. Photon.* **11**, 441–446 (2017).
- Arrazola, J. M. et al. Quantum circuits with many photons on a programmable nanophotonic chip. *Nature* **591**, 54–60 (2021).
- Rogers, C. et al. A universal 3D imaging sensor on a silicon photonics platform. *Nature* **590**, 256–261 (2021).
- Watts, M. R. et al. Adiabatic thermo-optic Mach–Zehnder switch. *Opt. Lett.* **38**, 733–735 (2013).
- Thomson, D. J. et al. 50-Gb/s silicon optical modulator. *IEEE Photon. Technol. Lett.* **24**, 234–236 (2012).
- Bogaerts, W. et al. Programmable photonic circuits. *Nature* **586**, 207–216 (2020).
- Han, J.-H. et al. Efficient low-loss InGaAsP/Si hybrid MOS optical modulator. *Nat. Photon.* **11**, 486–490 (2017).
- He, M. et al. High-performance hybrid silicon and lithium niobate Mach–Zehnder modulators for 100 Gbit s⁻¹ and beyond. *Nat. Photon.* **13**, 359–364 (2019).
- Koerber, S. et al. Femtojoule electro-optic modulation using a silicon–organic hybrid device. *Light Sci. Appl.* **4**, e255 (2015).
- Rudolph, T. Why I am optimistic about the silicon-photonic route to quantum computing. *APL Photon.* **2**, 030901 (2017).
- Fang, Z., Chen, R., Zheng, J. & Majumdar, A. Non-volatile reconfigurable silicon photonics based on phase-change materials. *IEEE J. Sel. Top. Quantum Electron.* <https://doi.org/10.1109/JSTQE.2021.3120713> (2021).
- Raoux, S., Xiong, F., Wuttig, M. & Pop, E. Phase change materials and phase change memory. *MRS Bull.* **39**, 703–710 (2014).
- Shportko, K. et al. Resonant bonding in crystalline phase-change materials. *Nat. Mater.* **7**, 653–658 (2008).
- Zheng, J. et al. Nonvolatile electrically reconfigurable integrated photonic switch enabled by a silicon PIN diode heater. *Adv. Mater.* **32**, 2001218 (2020).
- Zheng, J. et al. GST-on-silicon hybrid nanophotonic integrated circuits: a non-volatile quasi-continuously reprogrammable platform. *Opt. Mater. Express* **8**, 1551–1561 (2018).
- Ríos, C. et al. Ultra-compact nonvolatile photonics based on electrically reprogrammable transparent phase change materials. Preprint at <https://arxiv.org/abs/2105.06010> (2021).
- Xu, P., Zheng, J., Doyle, J. K. & Majumdar, A. Low-loss and broadband nonvolatile phase-change directional coupler switches. *ACS Photon.* **6**, 553–557 (2019).
- Ríos, C. et al. Integrated all-photonic non-volatile multi-level memory. *Nat. Photon.* **9**, 725–732 (2015).
- Feldmann, J. et al. Calculating with light using a chip-scale all-optical abacus. *Nat. Commun.* **8**, 1256 (2017).
- Feldmann, J. et al. Parallel convolutional processing using an integrated photonic tensor core. *Nature* **589**, 52–58 (2021).
- Delaney, M. et al. Nonvolatile programmable silicon photonics using an ultralow-loss Sb₂Se₃ phase change material. *Sci. Adv.* **7**, eabg3500 (2021).
- Delaney, M., Zeimpekis, I., Lawson, D., Hewak, D. W. & Muskers, O. L. A new family of ultralow loss reversible phase-change materials for photonic integrated circuits: Sb₂S₃ and Sb₂Se₃. *Adv. Funct. Mater.* **30**, 2002447 (2020).
- Zheng, J., Zhu, S., Xu, P., Dunham, S. & Majumdar, A. Modeling electrical switching of nonvolatile phase-change integrated nanophotonic structures with graphene heaters. *ACS Appl. Mater. Interfaces* **12**, 21827–21836 (2020).
- Zhang, H. et al. Miniature multilevel optical memristive switch using phase change material. *ACS Photon.* **6**, 2205–2212 (2019).
- Kato, K., Kuwahara, M., Kawashima, H., Tsuruoka, T. & Tsuda, H. Current-driven phase-change optical gate switch using indium–tin-oxide heater. *Appl. Phys. Express* **10**, 072201 (2017).
- Taghinejad, H. et al. ITO-based microheaters for reversible multi-stage switching of phase-change materials: towards miniaturized beyond-binary reconfigurable integrated photonics. *Opt. Express* **29**, 20449–20462 (2021).
- Fang, Z. et al. Non-volatile reconfigurable integrated photonics enabled by broadband low-loss phase change material. *Adv. Opt. Mater.* **9**, 2002049 (2021).
- Xiong, F., Liao, A. D., Estrada, D. & Pop, E. Low-power switching of phase-change materials with carbon nanotube electrodes. *Science* **332**, 568–570 (2011).

31. Khan, A. I. et al. Ultralow-switching current density multilevel phase-change memory on a flexible substrate. *Science* **373**, 1243–1247 (2021).
32. Farmakidis, N. et al. Plasmonic nanogap enhanced phase-change devices with dual electrical-optical functionality. *Sci. Adv.* **5**, eaaw2687 (2019).
33. Ballan, H. & Declercq, M. *High Voltage Devices and Circuits in Standard CMOS Technologies* (Springer, 2013).
34. Moss, D. J., Morandotti, R., Gaeta, A. L. & Lipson, M. New CMOS-compatible platforms based on silicon nitride and Hydex for nonlinear optics. *Nat. Photon.* **7**, 597–607 (2013).
35. Heimala, P., Katila, P., Aarnio, J. & Heinamaki, A. Thermally tunable integrated optical ring resonator with poly-Si thermistor. *J. Lightwave Technol.* **14**, 2260–2267 (1996).
36. Fang, Z., Zheng, J., & Majumdar, A. Non-volatile integrated photonics enabled by broadband transparent phase change material. In *Conference on Lasers and Electro-Optics JTh2B.3* (Optical Society of America, 2020); https://doi.org/10.1364/CLEO_AT.2020.JTh2B.3
37. Ríos, C. et al. Multi-level electro-thermal switching of optical phase-change materials using graphene. *Adv. Photon. Res.* **2**, 2000034 (2021).
38. Ríos, C. et al. In-memory computing on a photonic platform. *Sci. Adv.* **5**, eaau5759 (2019).
39. Loke, D. K. et al. Ultrafast nanoscale phase-change memory enabled by single-pulse conditioning. *ACS Appl. Mater. Interfaces* **10**, 41855–41860 (2018).
40. Xiong, C. et al. Monolithic 56 Gb/s silicon photonic pulse-amplitude modulation transmitter. *Optica* **3**, 1060–1065 (2016).
41. Schuler, S. et al. High-responsivity graphene photodetectors integrated on silicon microring resonators. *Nat. Commun.* **12**, 3733 (2021).
42. Wang, F. et al. Gate-variable optical transitions in graphene. *Science* **320**, 206–209 (2008).
43. Soriano, V. et al. Graphene–silicon phase modulators with gigahertz bandwidth. *Nat. Photon.* **12**, 40–44 (2018).
44. Li, X. et al. Fast and reliable storage using a 5 bit, nonvolatile photonic memory cell. *Optica* **6**, 1–6 (2019).
45. Wang, L. et al. One-dimensional electrical contact to a two-dimensional material. *Science* **342**, 614–617 (2013).
46. Gao, L. et al. Face-to-face transfer of wafer-scale graphene films. *Nature* **505**, 190–194 (2014).
47. Lee, Y. et al. Wafer-scale synthesis and transfer of graphene films. *Nano Lett.* **10**, 490–493 (2010).
48. Romagnoli, M. et al. Graphene-based integrated photonics for next-generation datacom and telecom. *Nat. Rev. Mater.* **3**, 392–414 (2018).

Publisher's note Springer Nature remains neutral with regard to jurisdictional claims in published maps and institutional affiliations.

© The Author(s), under exclusive licence to Springer Nature Limited 2022

Methods

Device fabrication. The graphene-PCM photonic switch was fabricated on a 220-nm-thick silicon layer on top of a 3- μm -thick buried oxide layer (SOITECH). Supplementary Fig. 1 shows the schematics of fabrication flow. The pattern was defined by a JEOL JBX-6300FS 100kV electron-beam lithography (EBL) system using a positive tone ZEP-520A resist. The 220 nm fully etched ridge waveguides were prepared by inductively coupled plasma reactive ion etching (ICP-RIE) in fluorine-based gases. Before removing the resists, 220 nm SiO_2 was evaporated onto the resist-coated waveguides by electron-beam evaporation. The lift-off of SiO_2 was completed by sonication in methylene chloride for 3 min, which led to planarized waveguides. Then, 10 nm thermal ALD Al_2O_3 (H_2O precursor at 150 °C) was grown on the substrate to prevent the formation of a semiconductor and metal junction between the graphene and silicon. A second EBL step using a positive tone poly(methyl methacrylate) (PMMA) resist was subsequently carried out to create windows for the deposition of Ti/Au. After development, 5 nm Ti followed by 100 nm Au were deposited onto the chip by electron-beam evaporation. The Ti/Au was lifted off by immersing the chip in methylene chloride. Monolayer graphene (Graphenea) grown by chemical vapour deposition was transferred onto the chip by the standard PMMA wet transfer technique⁴⁹ and then patterned by EBL using a maN 2403 negative resist. Then, O_2 plasma was used to etch away the graphene that was not protected by the resist, followed by deposition of another 10 nm thermal ALD Al_2O_3 capping layer to protect the graphene during the subsequent fabrication steps. The high quality of the transferred graphene in the fabricated devices was confirmed by Raman spectroscopy (Supplementary Fig. 8). A fourth EBL overlay step was conducted to expose the PMMA resist before depositing GST or Sb_2Se_3 by magnetron sputtering. Then, 23 nm GST was deposited by magnetron sputtering (Lesker Lab 18) using a GST target at 28 W d.c. power and a base pressure of $\sim 5 \times 10^{-7}$ torr. The Ar flow rate was controlled to maintain a sputtering pressure of 3.5 mtorr. Sb_2Se_3 was deposited using a magnetron sputtering system at 30 W radiofrequency (RF) power under a deposition pressure of 4 mtorr and an Ar flow of $30 \text{ cm}^3 \text{ min}^{-1}$. The deposition rate for Sb_2Se_3 was $\sim 1 \text{ nm min}^{-1}$. Additionally, the samples were capped with 10 nm SiO_2 sputtered in situ (150 W RF power, 4 mtorr pressure and an Ar flow of $30 \text{ cm}^3 \text{ min}^{-1}$) to prevent oxidation during sample shipping. For the selenide deposition, the sputtering chamber was subjected to several pre-deposition and post-deposition treatments, including cleaning the chamber followed by annealing and cleaning with O_2 plasma. Prior to Sb_2Se_3 deposition, the sputtering chamber was baked at 400 °C for 6 h (under vacuum), followed by cooling to room temperature to drive out gases and other contaminants. The toxic residual hydrogen selenide formed during Sb_2Se_3 deposition was removed by flowing O_2 plasma for 1 h prior to opening the sputtering chamber. The atomic ratio of Sb_2Se_3 after deposition was confirmed by X-ray photoelectron spectroscopy to be $\text{Sb}/\text{Se} \approx 44:56$, which is close to the sputtering target stoichiometry of $\text{Sb}/\text{Se} \approx 40:60$. Immediately after lifting off the PCM in methylene chloride, a 40 nm ALD Al_2O_3 layer was grown on the chip to protect the PCM from oxidation and reflowing during switching. To allow good electrical contact between the probes and the metal pads, a fifth EBL step was performed to open windows in the PMMA resist at the contact regions for Al_2O_3 etching. The Al_2O_3 on top of the contacts was etched away by ICP-RIE in chlorine-based gases. Finally, the PCMs were initialized into the fully crystalline state by rapid thermal annealing at 200 °C for 10 min under N_2 atmosphere before measurement. The patterned graphene did not peel off after subsequent fabrication steps owing to its protection by 10 nm ALD alumina.

Experimental set-up and measurements. The waveguides and micro-rings were characterized using a vertical fibre-coupling set-up¹⁶. All the measurements were performed under ambient conditions, with the temperature of the stage fixed at ~ 26 °C by a thermoelectric controller (TE Technology, TC-720) to prohibit a serious thermal shift of the resonators. The input light was provided by a tunable continuous-wave laser (Santec, TSL-510) and its polarization was controlled by a manual fibre polarization controller (Thorlabs, FPC526) to match the fundamental quasi-transverse-electric mode of the waveguides.

A low-noise power meter (Keysight, 81634B) was used to collect the static optical output from the grating couplers. Transmission spectra were recorded after the fabrication of bare micro-rings, deposition of the metal, transfer of the SLG and deposition of Sb_2Se_3 to determine the change in optical losses in each step. In the electrical characterization, electrical signals were applied to the metal contacts through a pair of d.c. probes controlled by two probe positioners (Cascade Microtech, DPP105-M-AI-S). The voltage sweep and current measurements were conducted using a source meter (Keithley, 2450). The generated current-voltage (I - V) curves were used to estimate the power of the applied pulses. The SET and RESET pulses were generated by a pulse function arbitrary generator (Keysight, 81150A). To reconfigure the graphene-GST photonic switch, we used a 5 V voltage pulse (2.78 mA), 400 ns pulse width and 8 ns rising/trailing edge to induce

amorphization. For crystallization, a 3 V voltage pulse (1.79 mA), 100 μs pulse width and 120 μs trailing edge were used. To reconfigure the graphene- Sb_2Se_3 phase shifter, we used a 6.8 V voltage pulse (3.4 mA), 400 ns pulse width and 8 ns rising/trailing edge to induce amorphization. For crystallization, a 4 V voltage pulse (2.0 mA), 100 μs pulse width and 120 μs trailing edge were used. The voltage was the actual voltage applied across the device as the impedance was matched by setting the load impedance of the function generator to the total resistance of the device determined from the I - V curve. The graphene could withstand a maximum current typically of around 3 mA in our experiments. To perform the endurance test shown in Fig. 3e, the laser wavelength was initially parked near the resonance, which gives a larger optical contrast, but later drifts away from the resonance, leading to a simultaneous increase in transmission in both states and a slightly decreased contrast. The data were filtered by a 50-point moving average to reduce the fluctuation caused by thermal noise. The resonance drift of high- Q resonators due to temperature variation in the surroundings is not an uncommon issue due to the relatively strong thermo-optic effect of silicon, and integrated metallic heaters near the resonators are normally used to stabilize the temperature^{50,51}. Optimized thermal stabilization is beyond the scope of this paper and will be explored in future work. To measure the transient response of the switch (Supplementary Fig. 9), the output light from the grating couplers was amplified using an optical fibre amplifier (Amonics, AEDEFA-30-B-FA), and the amplified signal was detected with a 150 MHz near-infrared fast photoreceiver (Thorlabs, PDB450C) connected to an oscilloscope.

Data availability

The data that support the findings of this study are available from the corresponding authors upon reasonable request.

References

- Liang, X. et al. Toward clean and crackless transfer of graphene. *ACS Nano* **5**, 9144–9153 (2011).
- Atabaki, A. H. et al. Integrating photonics with silicon nanoelectronics for the next generation of systems on a chip. *Nature* **556**, 349–354 (2018).
- Sun, C. et al. Single-chip microprocessor that communicates directly using light. *Nature* **528**, 534–538 (2015).

Acknowledgements

This research was funded by the National Science Foundation (NSF-1640986 and NSF-2003509), an ONR-YIP Award, a DARPA-YFA Award, the Draper Laboratory and Intel. Part of this work was conducted at the Washington Nanofabrication Facility/Molecular Analysis Facility, a National Nanotechnology Coordinated Infrastructure (NNCI) site at the University of Washington with partial support from the National Science Foundation (NNCI-1542101 and NNCI-2025489). We thank S. Moazeni for allowing us to use the high-speed photoreceiver at the University of Washington.

Author contributions

Z.F. and A.M. conceived the project. Z.F. simulated, designed and fabricated the devices. Z.F. led the switching experiments, optical characterizations and performed the data analysis. R.C. helped with the experiments and characterizations. J.Z. developed the initial fabrication process flow and design of the experiments. J.Z. and R.C. helped with the data analysis. A.I.K. and K.M.N. deposited the Sb_2Se_3 materials. A.S. illustrated the device schematics. M.E.C. advised on the SLG transfer process. C.R. and J.H. advised on the device design and fabrication process. E.P. facilitated the Sb_2Se_3 deposition and advised on the transfer of SLG. A.M., S.J.G., D.M.C. and M.G.M. supervised the overall progress of the project. Z.F. wrote the manuscript with input from all the authors.

Competing interests

All authors are listed as co-inventors on a US patent provisional application (patent application number 63/365,135) on the ultra-low-energy phase shifter filed by the Charles Stark Draper Laboratory.

Additional information

Supplementary information The online version contains supplementary material available at <https://doi.org/10.1038/s41565-022-01153-w>.

Correspondence and requests for materials should be addressed to Zhuoran Fang or Arka Majumdar.

Peer review information *Nature Nanotechnology* thanks Otto Muskens and Linjie Zhou for their contribution to the peer review of this work.

Reprints and permissions information is available at www.nature.com/reprints.